Electronic supplementary information

Layered structures and nanosheets of pyrimidinethiolate coordination polymers

P. J. Beldon, S. Tominaka, P. Singh, T. Saha Dasgupta, E. G. Bithell & A. K. Cheetham

Contents

Experimental methods

Nickel(II) acetate tetrahydrate (99.998%), iron(II) acetate (99.995%) and 2-Mercaptopyrimidine (98%) were purchased from Sigma Aldrich and were used without further purification. Nickel(II) sulfate hexahydrate (99%) and isopropanol (99.8%) were purchased from Acros and used without further purification. N,N-Dimethylformamide (HPLC grade), methanol (lab reagent grade), dimethyl sulfoxide (analytical reagent grade), and water (analytical reagent grade) were purchased from Fisher and used without further purification.

Synthesis of $[Ni(Py2th)_2]_n$

Nickel (II) acetate tetrahydrate (1eq, 49.8 mg, 0.2 mmol) and pyrimidine-2-thiol (2 eq, 44.9 mg, 0.4 mmol) were placed into in a 23 ml PTFE-lined, stainless steel autoclave with 10 ml methanol. The autoclave was sealed and placed in an oven at 90°C for 12 h. After this time, the autoclave was removed from the oven and allowed to cool to room temperature. The mother liquor was pipetted off and the crystals were washed several times with dimethyl sulfoxide. The crystals were separated by Buchner filtration and washed on the filter with dimethyl sulfoxide (DMSO) and methanol. $[Ni(Py2th)_2]_n$ (40 mg, 0.14 mmol, 71%) was recovered as green, hexagonal platelet crystals. Elemental analysis: Calculated mass %: C 34.16; H 2.15; N 19.92; Ni 20.96; S 22.80. Found mass %: C 34.05; H 2.26; N 19.30.

Synthesis and structure determination of $[Fe(Py2th)_2]_n$

Iron (II) acetate (1eq, 104.4 mg, 0.6 mmol) and pyrimidine-2-thiol (2 eq, 134.7 mg, 1.2 mmol) were placed into in a 100 ml round bottom flask and the flask was degassed and backfilled with nitrogen 3 times. Then, the mixed powder was dissolved with 45 ml of a methanol–isopropanol mixture (3:1 v/v), which had been deaerated by bubbling with nitrogen for 20 minutes. The mixture was bubbled with nitrogen for a further 5 minutes; the flask was then sealed and placed in an oven at 90°C for 12 h. The mother liquor was pipetted off and the crystals were washed several times with DMSO. The crystals were separated by Buchner filtration and washed on the filter with DMSO and methanol. $[Fe(Py2th)_2]_n$ (92 mg, 0.33 mmol, 55%) was recovered as red, block crystals. Elemental analysis: Calculated mass %: C 34.55; H 2.17; N 20.14; Fe 20.08; S 23.06. Found mass %: C 34.42; H 2.25; N 19.54.

Single crystal diffraction data was collected on $[Fe(Py2th)_2]_n$ at 293.0 K using an Oxford Diffraction Gemini Ultra diffractometer. Using Olex2[1], the structure was solved with the ShelXS[2] structure solution program using Direct Methods and refined with the ShelXL[2] refinement package using Least Squares minimisation.

Crystal data for $[Fe(Py2th)_2]_n$ (M =278.14): orthorhombic, space group Pbca (no. 61), a = 7.90952(17) Å, b = 16.0335(4) Å, c = 15.9946(3) Å, V = 2028.39(8) Å^3, Z = 8, T = 293.0 K, μ(Cu Kα) = 15.522 mm^{-1}, $Dcalc$ = 1.822 g/mm^3, 10617 reflections measured ($11.036 \leq 2\theta \leq 140.468$), 1928 unique ($R_{int}$ = 0.0554) which were used in all calculations. The final R_1 was 0.0396 ($I > 2\sigma(I)$) and wR_2 was 0.1115 (all data).

Synthesis of brown phase

Nickel (II) sulfate hexahydrate (1eq, 15.8 mg, 0.06 mmol) and pyrimidine-2-thiol (2 eq, 13.5 mg, 0.12 mmol) were placed into in a 20 ml glass vial. This mixture was dissolved in a dimethylformamide–water mixture (10 ml, 1:9 v/v). The vial was sealed and placed in an oven at 90°C for 12 h, and then allowed to cool to room temperature. The crystals were separated by Buchner filtration and washed on the filter with DMSO and methanol. The brown phase (2 mg) was recovered as brown, needle-like crystals with a small amount of $[Ni(Py2th)_2]_n$ as an impurity.

Single crystal diffraction data was collected via the national Crystallography service at I19 at the Diamond Light Source. Unfortunately the structure could not be solved satisfactorily.

Conductivity measurements

Conductivities were measured by the AC impedance method using an electrochemical instrument (Gamry Interface 1000) in the frequency range of 1 MHz to 0.01 Hz. In order to examine materials with high resistance, a relatively large AC amplitude of 100 mV was used. The data were analyzed on the basis of an equivalent circuit shown in Fig. S3d. When measuring electrical conductivity, there is always some leakage current through the instrument or the cell, known as the dark current. Thus, the setup has an apparent resistance, even with no sample in place (2.9 TΩ at 30°C in our setup). This sets the detection limit of the measurement: samples with a resistance higher than the apparent resistance of the setup cannot be measured.

Powder conductivity measurements were carried out using a commercially available cell with brass electrodes covered with thin gold layer (EQ-STC 10 mm, MTI Corporation, USA). To prepare pressed-powder pellets for conductivity measurements, the samples were gently ground to a fine powder using a pestle and mortar. Approximately 80 mg of this fine powder was placed in a

10 mm diameter die and subjected to a 2 ton load for 10 minutes in a pellet press. The thickness of each pellet was measured using callipers.

Single-crystal conductivity measurements were carried our using a homemade setup composed of gold microelectrodes with a spacing of 80 μm prepared on a quartz substrate using photolithography and evaporation, as reported previously.[3] Individual crystals were mounted across the electrodes and secured in place using electrically insulating, silicone adhesive tape. In contrast to the powder measurements, this process can mount the single crystals delicately. Since the crystals are fragile, we checked the condition of the crystals by optical microscopy before and after the measurement. Electrical contact between single crystals and microelectrodes was confirmed by control experiments using tetrathiafulvalene nitrate crystals.[3] For $[Ni(Py2th)_2]_n$ and $[Fe(Py2th)_2]_n$ the conductivity was measured in numerous directions within the lamellar plane. For the brown phase, the conductivity was measured along the long axis of the needle crystals.

Characterisation of nanosheets by TEM and AFM

$[Ni(Py2th)_2]_n$ or $[Fe(Py2th)_2]_n$ (50 mg) was exfoliated by sonication in ethanol (5 ml) and left to stand for 18 hours. The resulting suspension showed strong Tyndall scattering when a laser was shone through the sample. Taking care not to disturb the sediment, this suspension was deposited onto a substrate (2 μl onto single-crystal Al_2O_3 for AFM, or 20 μl onto a holey carbon TEM grid for TEM). Tapping mode AFM was performed using a Veeco Dimension 3100 AFM. Images were flattened using a second order plane fitting. TEM analysis was performed using a Philips (FEI) CM30 transmission electron microscope, operating at 300kV, and without sample cooling. Bright field images and selected area diffraction patterns were recorded on high dynamic range Ditabis imaging plates. Analysis of the electron diffraction was performed using CrystalMaker®/SingleCrystal™, CrystalMaker Software Ltd, Oxford, England (www.crystalmaker.com).

DFT calculations

The density functional theory (DFT) based calculations have been performed within the generalized gradient approximation (GGA)[4] of the exchange-correlation functional with the choice of Perdew-Burke-Ernzerhof (PBE) functional[5] in a spin polarized scheme. To improve the description of correlation effects in the d electrons of Ni and Fe, we used a DFT+U[6,7] method within an approach due to Dudarev et al.[8] The effect of variation of U_{eff} on the trend in calculated electronic structure was found to be minimal, though as expected, increasing the value of U_{eff} increases the gap value. The calculations were performed using a plane wave basis as implemented in the Vienna Ab-initio Simulation Package (VASP).[9–11] For these plane wave calculations, we used projector augmented wave (PAW) potentials[12] and the wave functions were expanded in the plane wave basis with a kinetic energy cutoff of 400 eV. Reciprocal space integrations were carried out with a k mesh of 8 x 4 x 4. The crystal structures were optimized starting from the experimentally measured structures, fixing the lattice constants at experimentally determined values, until the total forces on each ion were converged to better than 0.01 eV/Å. For the density of states calculations, a Gaussian smearing of 0.1 eV was used.

Comparison of the structures of $[Fe(Py2th)_2]_n$ and $[Ni(Py2th)_2]_n$

In $[Fe(Py2th)_2]_n$, the metal octahedra are more distorted than in $[Ni(Py2th)_2]_n$ and this manifests as a contraction of the c axis despite the expected overall volume expansion (Table S1).

Table S1 Structural parameters of $[Fe(Py2th)_2]_n$ compared to $[Ni(Py2th)_2]_n$

	$[Fe(Py2th)_2]_n$	$[Ni(Py2th)_2]_n$
Space group	Pbca	Pbca
a/Å	7.90952(17)	7.8860(6)
b/Å	16.0335(4)	15.5844(11)
c/Å	15.9946(3)	16.2399(12)
Volume/Å^3	2028.39(8)	1995.861

PXRD data for $[Ni(Py2th)_2]_n$ and the brown phase

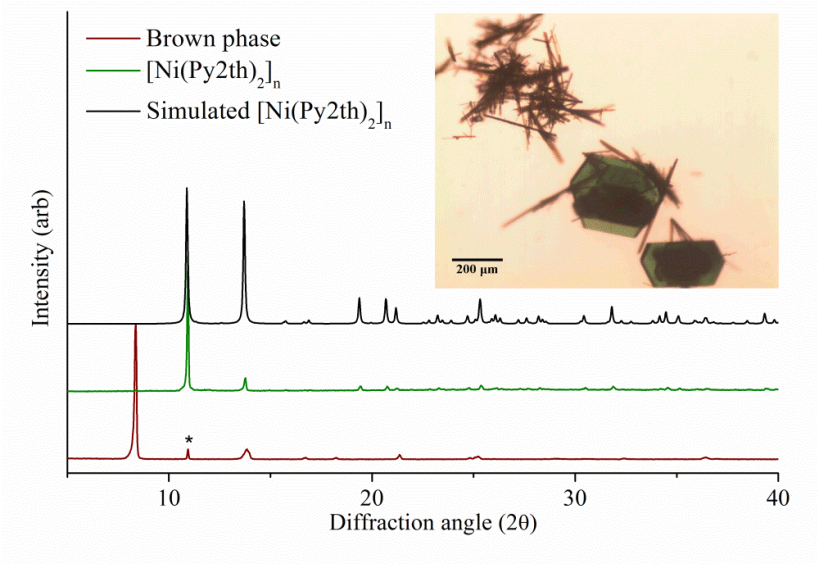

Figure S1 Simulated and experimental PXRD patterns of $[Ni(Py2th)_2]_n$. Experimental pattern for the brown phase with an impurity peak from $[Ni(Py2th)_2]_n$ highlighted*. Inset: Optical microscopy images of $Ni(Py2th)_2]_n$ and the brown phase, present after reaction between nickel (II) acetate & pyrimidine-2-thiol.

PXRD data for $[Fe(Py2th)_2]_n$

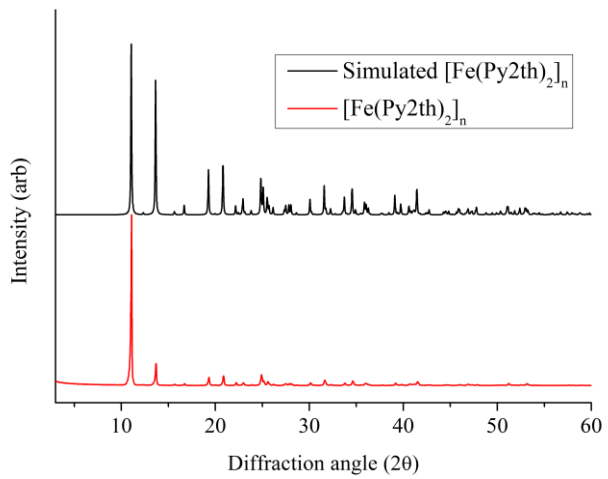

Figure S2 Simulated and experimental PXRD patterns of $[Fe(Py2th)_2]_n$.

AC impedance analysis

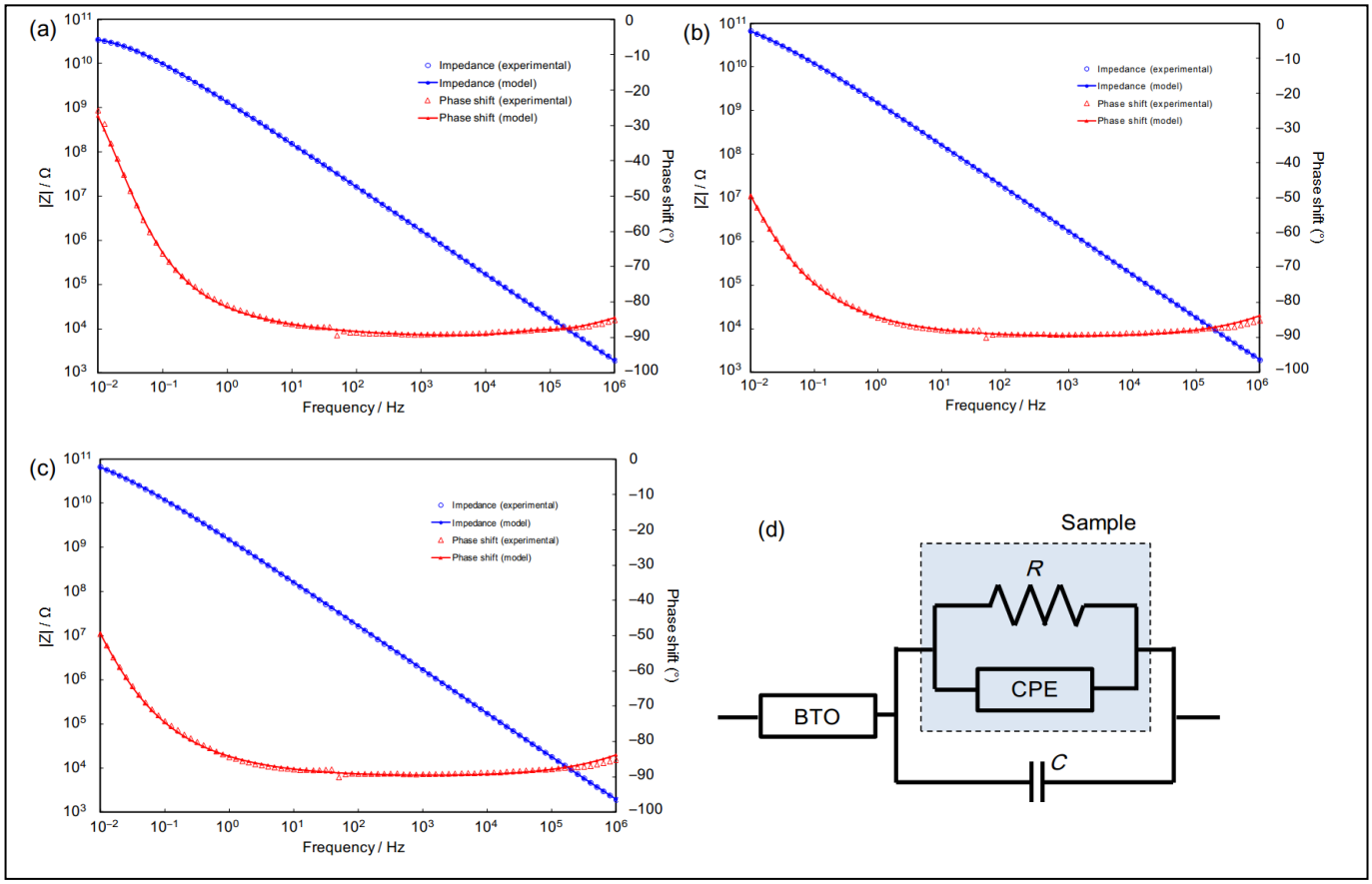

Figure S3 Bode plots of the AC impedance data for (a) $[Fe(Py2th)_2]_n$, (b) $[Ni(Py2th)_2]_n$ and (c) brown phase. The experimental data were collected by applying AC amplitude of 100 mV from 1 M Hz to 10 mHz, and then were analyzed by curve fitting using the equivalent circuit shown in Panel 'd'. The equivalent circuit includes contributions from the sample and the apparatus. The sample contribution is a resistance associated with bulk electronic resistance in parallel with a constant phase element associated with the dielectric constant and anisotropy of the sample-electrode interface. The apparatus contribution is a capacitor associated with a geometric capacitance of the cell and a transmission line (Bisquert model: Bisquert,J. J. Phys. Chem. B 2002, 106, 325-333), which represents floating capacitance.

The resistance for $[Fe(Py2th)_2]_n$ is 4.74×10^{10} ohm (b) $[Ni(Py2th)_2]_n$ is 1.83×10^{11} ohm and (c) brown phase is 1.23×10^{11} ohm. The pellet thickness for $[Fe(Py2th)_2]_n$ is 0.076 cm (b) $[Ni(Py2th)_2]_n$ is 0.064 cm and (c) brown phase is 0.021 cm. The pellet diameter is 1 cm for all samples.

UV/VIS data for $[Ni(Py2th)_2]_n$

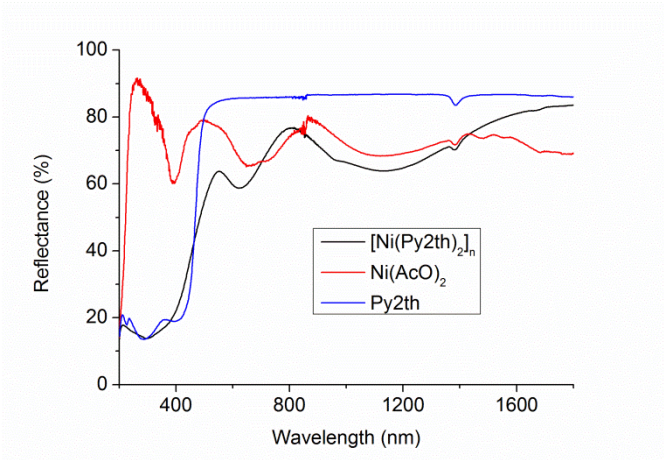

Figure S4 UV/VIS spectra of $[Ni(Py2th)_2]_n$, nickel (II) acetate and pyrimidine-2-thiol.

Spin-polarised DFT band structures for $[Ni(Py2th)_2]_n$ and $[Fe(Py2th)_2]_n$

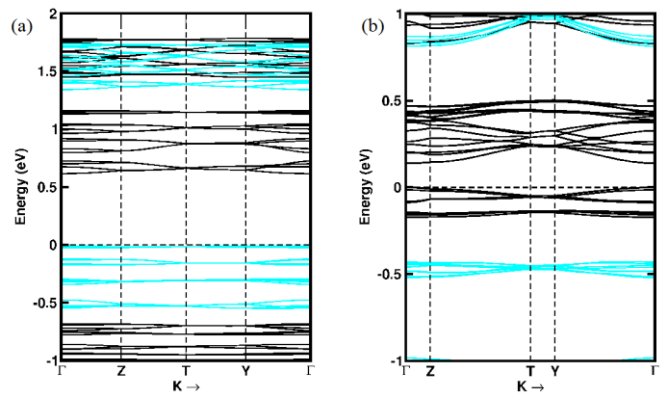

Figure S5 The calculated spin-polarized band structures of (a) $[Ni(Py2th)_2]_n$ and (b) $[Fe(Py2th)_2]_n$ plotted along the high symmetry points of the Brillouin zone. The spin-up and spin-down bands are shown in black and cyan colour, respectively. The zero of the energy scale is set to the Fermi energy. Both materials are insulators with a finite band gap and exhibit little band dispersion, suggesting low mobility of the charge carriers.

Transmission electron microscopy

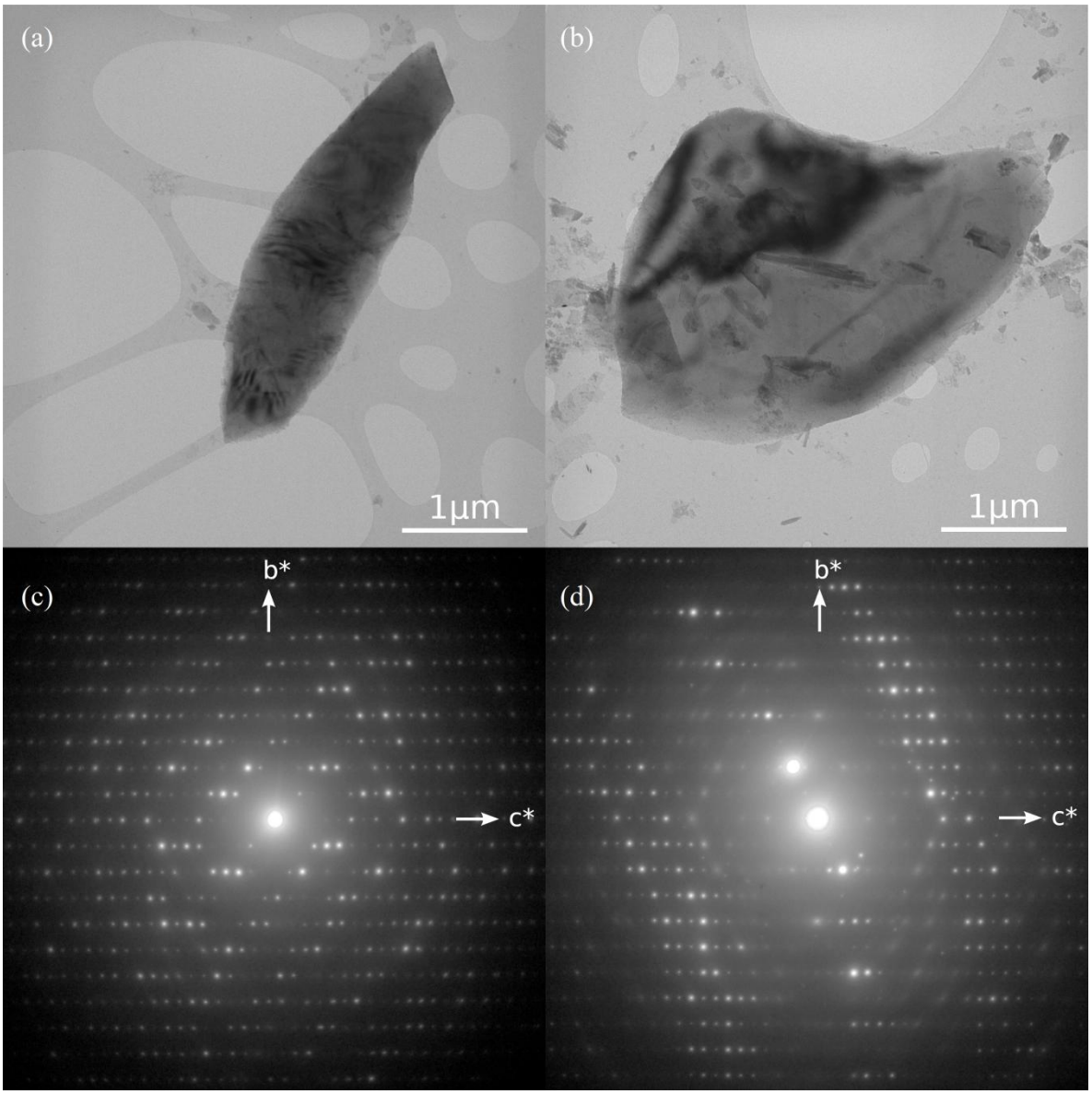

Figure S6 Two representative TEM images of clusters of the nanosheets and the selected area diffraction patterns for each one. (c) corresponds to (a), (d) corresponds to (b).

In the as-deposited orientation (i.e. without tilting the copper grid), most diffraction patterns are randomly misoriented from [001] by 5 – 15° (e.g. figs. 5c and 5d, corresponding to images 5a and 5b respectively). There is some evidence for bending of the sheets, but this is less pronounced than that observed in other exfoliated materials and in a less consistent crystallographic sense.[13] At the exact zone axis orientation, [001] is readily distinguished from [100] and [010], as a result of the glide systematic absences. The distinction is less straightforward under tilted conditions, when higher layer reflections begin to appear in the pattern. We have compared our experimental patterns with simulations of tilted orientations obtained using CrystalMaker®/SingleCrystal™, and have determined that our experimental patterns are consistent only with tilts away from the [001] zone axis. This assignment is consistent with the expected (001) exfoliation planes.

Despite the apparently high density of nanosheets in the suspension, the density of nanosheets deposited on the substrates (Al_2O_3 for AFM, carbon for TEM grid) was low. Often, only a single substantial sheet a few microns in diameter was found per 50 μm square. Each of these large sheets was invariably surrounded by smaller fragments (**Error! Reference source not found.**(d)). We

interpret this as a surface tension effect, suggesting that the sheets aggregate as the ethanol suspension evaporates, and that these aggregates do not adhere well to the substrate, depositing only a few discrete clusters. The dispersion of nanosheets on the surface may be improved by optimising the solvent.[14]

References

1. O. V. Dolomanov, L. J. Bourhis, R. J. Gildea, J. a. K. Howard, and H. Puschmann, *J. Appl. Crystallogr.*, 2009, **42**, 339–341.
2. G. M. Sheldrick, *Acta Crystallogr. A.*, 2008, **64**, 112–22.
3. S. Tominaka, S. Henke, and A. K. Cheetham, *CrystEngComm*, 2013, **15**, 9400–7.
4. J. P. Perdew, K. A. Jackson, M. R. Pederson, D. J. Singh, and C. Fiolhais, *Phys. Rev. B*, 1992, **46**, 6671–6687.
5. J. P. Perdew, K. Burke, and M. Ernzerhof, *Phys. Rev. Lett.*, 1996, **77**, 3865–3868.
6. V. I. Anisimov, J. Zaanen, and O. K. Andersen, *Phys. Rev. B*, 1991, **44**, 943–954.
7. A. I. Liechtenstein, V. I. Anisimov, and J. Zaanen, *Phys. Rev. B*, 1995, **52**, R5467–R5470.
8. S. L. Dudarev, S. Y. Savrasov, C. J. Humphreys, and A. P. Sutton, *Phys. Rev. B*, 1998, **57**, 1505–1509.
9. G. Kresse and J. Hafner, *Phys. Rev. B*, 1993, **47**, 558–561.
10. G. Kresse and J. Hafner, *Phys. Rev. B*, 1993, **48**, 13115–13118.
11. G. Kresse and J. Hafner, *Phys. Rev. B*, 1994, **49**, 14251–14269.
12. G. Kresse and D. Joubert, *Phys. Rev. B*, 1999, **59**, 1758–1775.
13. J.-C. Tan, P. J. Saines, E. G. Bithell, and A. K. Cheetham, *ACS Nano*, 2012, **6**, 615–21.
14. J. N. Coleman, M. Lotya, A. O'Neill, S. D. Bergin, P. J. King, U. Khan, K. Young, A. Gaucher, S. De, R. J. Smith, I. V Shvets, S. K. Arora, G. Stanton, H.-Y. Kim, K. Lee, G. T. Kim, G. S. Duesberg, T. Hallam, J. J. Boland, J. J. Wang, J. F. Donegan, J. C. Grunlan, G. Moriarty, A. Shmeliov, R. J. Nicholls, J. M. Perkins, E. M. Grieveson, K. Theuwissen, D. W. McComb, P. D. Nellist, and V. Nicolosi, *Science*, 2011, **331**, 568–71.